MIT Open Access Articles

Carbothermal Shock Synthesis of High Entropy Oxide Catalysts: Dynamic Structural and Chemical Reconstruction Boosting the Catalytic Activity and Stability toward Oxygen Evolution Reaction

Carbothermal Shock Synthesis of High Entropy Oxide Catalysts: Dynamic Structural and Chemical Reconstruction Boosting the Catalytic Activity and Stability toward Oxygen Evolution Reaction

Ali Abdelhafiz, Baoming Wang, Avetik R. Harutyunyan, and Ju Li*

Mixed transition-metals (TM) based catalysts have shown huge promise for water splitting. Conventional synthesis of nanomaterials is strongly constrained by room-temperature equilibria and Ostwald ripening. Ultra-fast temperature cycling enables the synthesis of metastable metallic phases of high entropy alloy nanoparticles, which later transform to oxide/hydroxide nanoparticles upon use in aqueous electrolytes. Herein, an in situ synthesis of non-noble metal high entropy oxide (HEO) catalysts on carbon fibers by rapid Joule heating and quenching is reported. Different compositions of ternary to senary (FeNiCoCrMnV) HEO nanoparticles show higher activity towards catalyzing the oxygen evolution reaction (OER) compared to a noble metal IrO_2 catalyst. The synthesized HEO also show two orders of magnitude higher stability than IrO_2, due to stronger carbide-mediated intimacy with the substrate, activated through the OER process. Alloying elements Cr, Mn and V affect OER activity by promoting different oxidation states of the catalytically active TM (Fe, Ni and Co). Dissolution of less stable elements (Mn, V and Cr) leads to enhancements of OER activity. Dynamic structural and chemical perturbations of HEO oxide nanoparticles activate under OER conditions, leading to enlargement in ECSA by forming mixed single atom catalysts and ultra-fine oxyhydroxide nanoparticles HEOs.

A. Abdelhafiz, A. R. Harutyunyan, J. Li
Department of Nuclear Science and Engineering
Massachusetts Institute of Technology
77 Massachusetts Avenue, Cambridge, MA 02139, USA
E-mail: liju@mit.edu
B. Wang, J. Li
Department of Materials Science and Engineering
Massachusetts Institute of Technology
77 Massachusetts Avenue, Cambridge, MA 02139, USA
A. R. Harutyunyan
Honda Research Institute USA, Inc
San Jose, CA 95134, USA

1. Introduction

Energy conversion technologies are crucial for the upcoming global energy transition. Intermittent electricity generated from solar and wind cannot be stored for prolonged periods due to limited grid-scale battery capacity.[1–3] Room-temperature water electrolyzer is a prime candidate to utilize intermittent electricity to produce hydrogen (and downstream chemicals and fuels) by water splitting.[4,5] Two major metrics are the capital cost and energy efficiency.[6] Also, a water electrolyzer is required to operate for thousands of hours, despite most of the current catalyst systems having 1–2 orders of magnitude shorter lifetime. Moreover, breakthroughs discovered on a laboratory scale suffer from scaling up challenges in manufacturing by orders of magnitude to match industrial demands.[7–9] Furthermore, the catalysts of choice are currently noble metal-based (Pt, Ru, or Ir) which are intrinsically resource-limited and render water electrolyzer less commercially competitive. Therefore, it is of great importance to come up with novel strategies to synthesize highly active, durable, and cost-effective electrocatalysts for room-temperature water electrolysis.

Anion exchange membrane electrolyzer cell (AEMEC) has shown huge promise for efficient hydrogen and oxygen production. Significant advancement has been made in the membrane and ionomer designs, which can operate for 2000 h.[8,9] On the contrary, most of the proposed catalysts in the literature suffer from low activity and short lifetime. Oxygen evolution reaction (OER) is the bottleneck for AEMEC and other electrochemical reactions, where the state-of-the-art catalyst used to date is IrO_2 (Iridium costs ≈ 10^5 kg^{-1}). Recent research showed that electrocatalysts designed by alloying two or more elements (e.g., transition metals, TM) showed promising enhancement in catalytic activity and durability due to synergistic effects from alloying, such as strain engineering or valence electron exchange.[4,10–15] Nevertheless, the full potential of the alloying approach is still constrained by standard synthesis methods (e.g., wet chemistry and thermal decomposition techniques) due to the thermodynamics rules (e.g., miscibility of the different alloying elements,

Ostwald ripening) for slow synthesis.[16,17] High entropy alloys (HEA), where more than three elements are alloyed together, are often complicated and tedious to achieve by conventional wet chemical methods.[18–25] One strategy to overcome this obstacle is to empower ultrafast kinetics to dictate the alloying formation. Rapid cycling of temperature from 25 °C to highly elevated temperature (1000–1700 °C), followed by cooling down to room temperature (RT) within a very short time scale (i.e., milli-second) for successive cycles, can stabilize metastable phases unachievable by slower synthesis methods. Carbothermal shock (CTS) synthesis relies on rapid Joule heating and quenching. As an electrical current passes through a substance and causes its temperature to rise rapidly, and then rapidly cool down due to the short thermal diffusion length, CTS is a great choice to achieve rapid temperature cycling. In addition to the alloy chemistry, enrichment of structural defects such as dislocations within the nanoparticles can be achieved by rapid cycling of temperature, which showed high activity toward different electrocatalytic reactions.[26–30] CTS has already shown great promise in synthesizing high entropy alloys and oxides nanoparticles of multiple elements which were known to be immiscible at the bulk scale by conventional methods.[31,32]

Herein, we report the utilization of CTS to synthesize non-noble TM highly active and durable electrocatalysts for OER in an alkaline aqueous medium. In the present work, we study the effect of incorporating different alloying elements (Cr, V, and Mn) with traditionally known promising catalysts (Ni, Fe, and Co) and their respective effect on the catalytic activity and durability of OER.

2. Results

2.1. Structure and Morphology

Spraying catalysts onto either the gas diffusion layer electrode (GDL) or electrolyte membrane is a cumbersome step that involves special apparatus and high catalyst waste (i.e., 30–50%) and produces rather superficial contacts between catalyst/GDL. In the present study, carbon fiber paper was chosen as a typical GDL used in actual AEMEC (Toray 60 with 5% wet proofing). The objective is to in situ synthesize OER catalyst directly attached to the substrate, and with strong intimacy onto the surface of carbon fibers of GDL without using any other binder/ionomer. We aim to achieve a strong interaction between catalyst and support (i.e., GDL), which results in stronger adhesion, that may work against capillary pulling forces from gas bubbles evolution which may erode off the catalyst during thousands of operating cycles.[33,34] In addition, in situ synthesis of the catalyst directly on GDL enables reducing the time and effort consumed to prepare a catalyst ink and coating many layers on GDL to make a membrane electrode assembly.

Our unique synthesis protocol starts with drop-casting of multi-metal chloride salts dissolved in ethanol at 50 mм concentration on a carbon fiber paper GDL. The total volume of the metal precursors solution was kept constant at 100 μL cm^{-2}(nominal area of GDL), and so the total TM loadings are also kept constant at 5 μmol (TM) cm^{-2}(nominal area of GDL). After solvent evaporation at RT overnight, GDL coated

with metal precursors were subjected to carbothermal (CTS) rapid joule heating. Electrical current of 15 A was applied for 3 pulses (500 ms). The electronic current passing through GDL raises its temperature to elevated levels (as high as ≈1300–1700 °C), as shown in the Figure S1, Supporting Information.[31] After 1.5 s, carbon fiber GDL was coated with HEA nanoparticles as represented in the schematic shown in **Figure 1**a. At high temperature, metal salts are first thermally reduced and then turn into liquid metal droplets, which are sitting on a carbon-rich environment (i.e., carbon fiber). Carbon has a very high diffusion rate in transition metals (e.g., Ni, Co, or Fe) dominated liquid or solid solutions. Thus, carbon is susceptible to being dissolved in the high-entropy multi-metallic liquid droplet. Quenching takes place within a fraction of a second to form a solid high entropy alloy nanoparticle. Dissolved carbon would have two options to either stay inside the lattice of HEA nanoparticle as octahedral interstitials, or to precipitate out as carbide.[35] The cooling rate is believed to be on the order of 5–10 °C ms^{-1}, which is long enough to allow for most of the carbon to precipitate out (carbon diffusivity ≈ 8×10^7 nm^2 ms^{-1}).[36,37] X-ray diffraction (XRD) analysis performed on pristine carbon fiber GDL (without any metal deposition) and after synthesis of HEA nanoparticles, showed no noticeable changes in the carbon peaks features. This may imply that carbon precipitates out from HEA NPs could be amorphous carbon, deposited at the interface between HEA NP and carbon fibers, as shown in the schematic in Figure 1a. In addition, X-rays are very penetrative, where the vast majority of the signal detected comes from the carbon fiber (≈1000 nm thick), which can screen the signal of the precipitated graphitic-carbon during HEA solidification.

Scanning electron microscopy (SEM) showed conformal coating of HEA catalyst nanoparticles on carbon fiber substrate. Coating was successfully achieved on carbon fibers from top to bottom across the GDL thickness. This is a desirable characteristic to maximize the performance per nominal area for AEMEC electrode, which is unachievable by conventional catalyst coating methods (e.g., using a spray air gun). Figure 1b–e shows SEM images of the conformal coating of HEA nanoparticles on carbon fiber, which shows progressive zoom-in version to show the morphology of HEA catalysts. Synthesized HEA nanoparticles range from 20 to 80 nm in diameter, while most particles have a diameter of 40–60 nm. Figure 1e shows that some particles (bottom right) formed trenches deep within the carbon fiber surface. This observation agrees with the proposed mechanism for strong intimate interaction between HEA and carbon support (Figure 1a) and can result in stronger nanoparticle adhesion. Initially metal chloride salts are heated up to vaporize Cl$_2$ and form a molten metal liquid droplet. Afterward, liquid molten metal droplets do particle "fission," etch the carbon substrate, and catalyze the reaction with scavenged oxygen functional groups from the carbon fiber surface, increasing the surface area, while molten metal droplets of different precursors fuse together and eventually reach fission-fusion balance at a quasi-steady state.[31,38] Carbon dissolution and carbide precipitation occur during heating and cooling cycles, respectively. In conventional synthesis methods (e.g., wet chemistry), weak superficial interaction (e.g., van der Waals forces) between carbon support and synthesized nanoparticles does not provide the necessary adhesion robustness
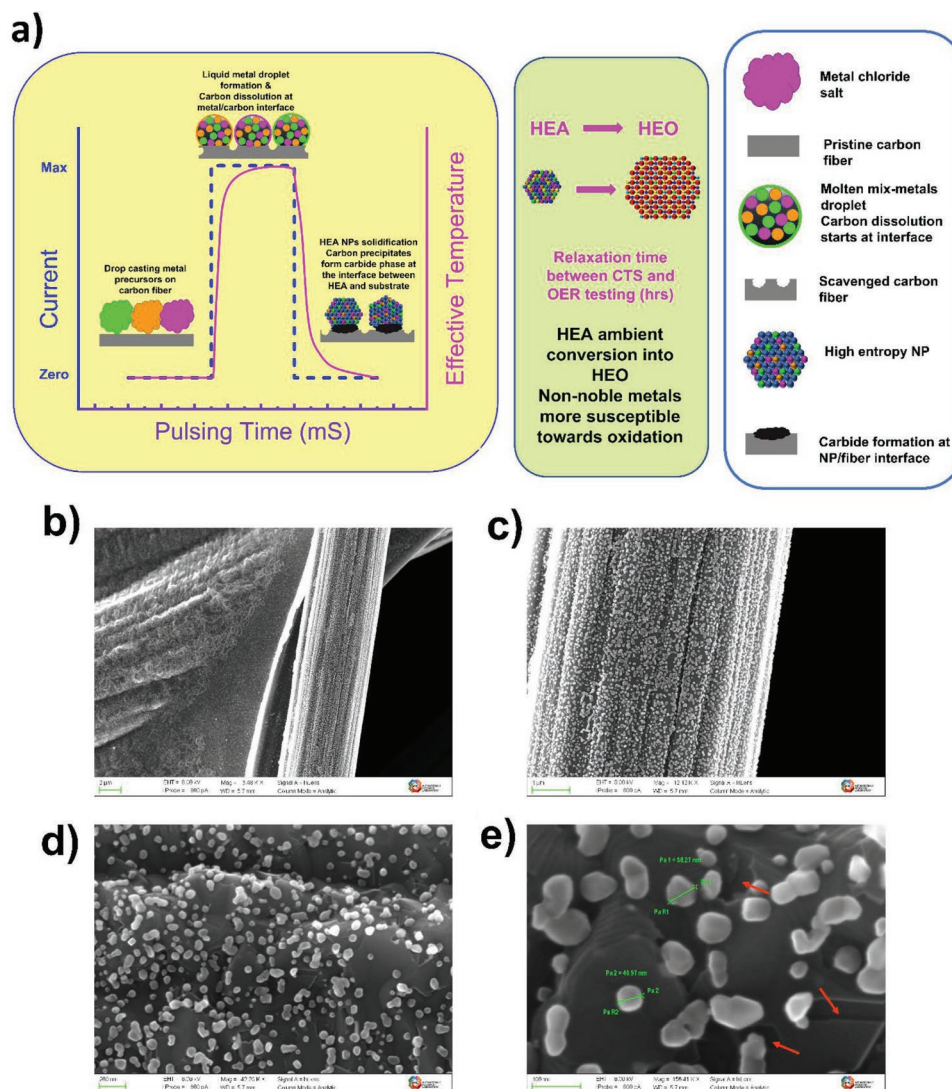
Figure 1. a) Schematic showing ultra-fast rapid Joule heating and spontaneous cooling process within mS pulse intervals. Process is shown as three stages depicted by cartoons: i) Dried metal precursors chunks on carbon fiber at room temperature. ii) Liquefaction of metal salts and carbon dissolution during joule heating. iii) Rapid cooling to room temperature to form HEA solid nanoparticles and carbon precipitation at the interface between HEA and carbon fiber. Following the synthesis process, HEA converts into HEO nanoparticles, before OER testing. b–e) SEM images on HEA catalyst nanoparticles synthesized on carbon fiber paper GDL, with zoom-in increasing from (b–e), successively, at the same location of the sample.

for prolonged service under gas bubbling conditions. Instead, our developed CTS synthesis provides a robust interaction between nanoparticles and carbon fiber, due to a strong metal-carbide bond formed due to the precipitation of carbides at the interface of NP/carbon fiber. This is expected to enhance the mechanical stability of the catalyst system against gas bubbles evolution during OER, with high capillary forces that may pull off catalysts from GDL (erosion).[39] Further data and analysis are presented in the following sections.

XRD analysis has been conducted to unravel the structural and chemical transformations due to different alloying and electrocatalytic testing conditions. The samples after synthesis maintained a spinel oxide crystal structure, commonly observed in literature for Fe/Ni/Co alloys.[40–47] Recent results presented in literature, and by this group, utilizing CTS to synthesize

nanoparticles showed formation of HEA when noble metals (e.g., Pt, Pd, and Au) were present in the HEA composition.[31] On the other hand, our presented study, herein, for exclusively non-noble metals chemistry (Fe, Ni, Co, Cr, Mn, and V) showed the formation of an oxide phase (i.e., high entropy oxide (HEO)), instead of metallic HEA. This may infer that the final state of the high entropy mixed metal particle upon solidification is chemistry dependent. Noble metals have higher resistance to oxidation, while non-noble metals can oxidize under ambient atmosphere easily. Another reason could be liberation of oxygen from carbon fibers during CTS, where non-noble metals are oxidized. Further experimental analysis is encouraged to fully understand the mechanism, which falls behind the scope of the presented study. Thus, hereon, nanoparticles synthesized in this study are referred to as HEO.
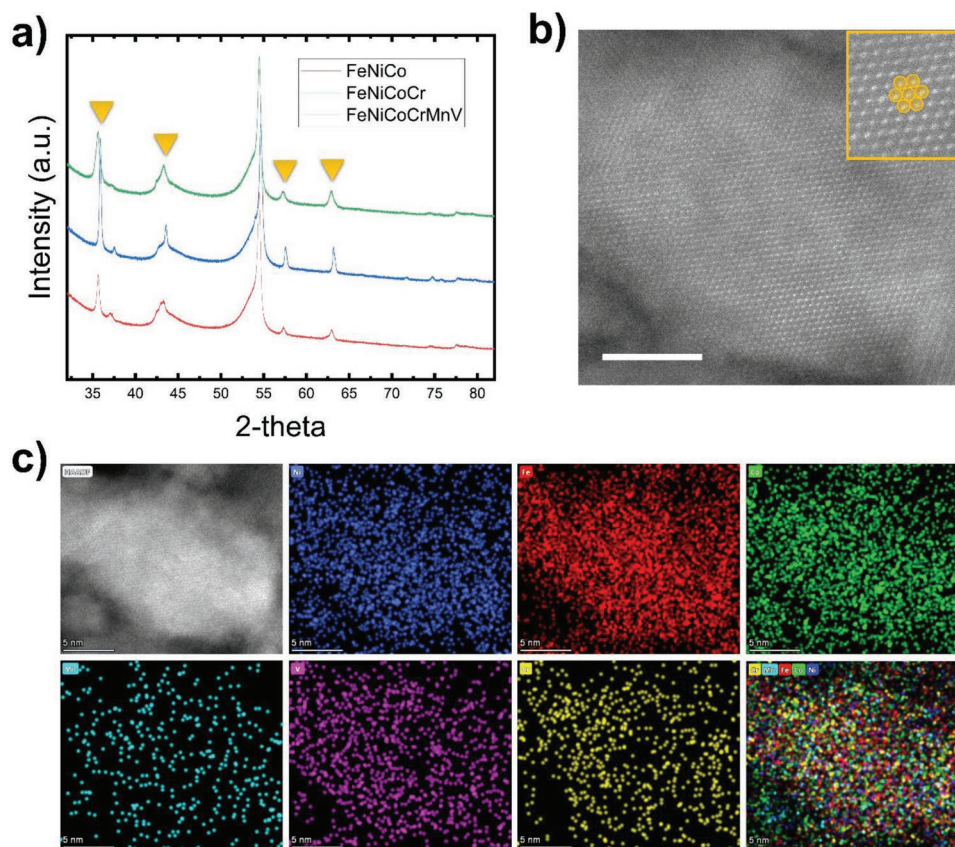
Figure 2. a) XRD spectra of FeNiCo, FeiCoCr, and FeNiCoCrMnV HEO catalysts (depicted in red, green, and blue, respectively), with yellow triangles pointing at the relevant peaks for spinel structure maintained by HEO catalyst. b,c) STEM imaging of FeNiCoCrMnV catalyst nanoparticles supported on carbon fiber paper. (b) STEM of FeNiCoCrMnV nanoparticles with and inset showing <111> crystal orientation. (c) STEM-HAADF image with corresponding EDX mapping panels for Fe (red), Ni (blue), Co (green), Cr (yellow), Mn (cyan), and V (magenta). The bottom right panel shows overlapping EDX maps to confirm the formation of HEO. Scale bar in (b) and (c) is 5 nm.

The peaks located at 27° and 54° are attributed to the carbon support. The spinel oxide structure has characteristic peaks located around 2θ angles of 35.6°, 63°, 30.5°, 57.5°, and 43.6°, where relative peak intensity follows the previous order systematically (from high to low). Our HEO catalysts FeNiCo, FeNiCoCr, and FeNiCoCrMnV spectra maintained the same spinel oxide structure, where peak positions and order or relative intensity remained intact, regardless of the alloying elements (i.e., Cr, Mn, or V), as shown in **Figure 2**a. Fundamentally, alloying different elements is expected to shift the position of the peaks to different 2θ values, due to differences in atomic radii of the alloying elements. The 3d transition metals (Fe, Ni, Co, Cr, Mn, and V) have slightly different ionic radii, which may not be clearly distinguishable with the limited resolution of the XRD machine. However, the addition of Cr to FeNiCo, forming FeNiCoCr, showed a slight shift to lower 2θ angles, as Cr ionic radius is larger than Fe, Ni, or Co. It is worth mentioning that no peak was detected for the single metal reflection (i.e., no unary phase segregation of Fe, Ni, Co, or Cr). Those observations confirmed the successful formation and dispersions of a HEO solid solution phase with the designed chemistries.

To further confirm the formation of HEO phase, samples were imaged by scanning transmission electron microscopy (STEM) followed by energy dispersive X-ray (EDX) mapping as shown in Figure 2b,c. Compared to SEM size distribution,

additional smaller particles were observed by STEM imaging with sizes below 10 nm. This implies that a particle imaged by SEM could be a cluster of a few smaller nanoparticles, which is hard to resolve with the limited SEM resolution. STEM imaging showed particles in different crystallographic orientations (e.g., <111>), as shown in Figure 2b. EDX elemental mapping was performed to unravel the distribution of each of the alloying elements, as shown in Figure 2c. Results showed a completely random distribution for all of the alloying elements, which is confirmed by an overlaid image. This confirms the successful formation of HEO nanoparticles. Mn mapping showed a slightly lower intensity than other elements, however still maintaining homogeneous random distribution across the particle. This observation indicates that Mn incorporation was successful, however at lower concentrations than expected from the precursor loading. This aligns with the fact that Mn salt (i.e., chloride) has a higher vapor pressure compared to other elements, where CTS at elevated temperatures (≈1300–1700 °C) may facilitate partial Mn vaporization.[48]

2.2. Electrocatalytic Activity

HEO catalysts supported on carbon-fiber GDL were tested in a three-electrode electrochemical setup to assess their

**ADVANCED
SCIENCE NEWS**

www.advancedsciencenews.com

**ADVANCED
ENERGY
MATERIALS**

www.advenergymat.de

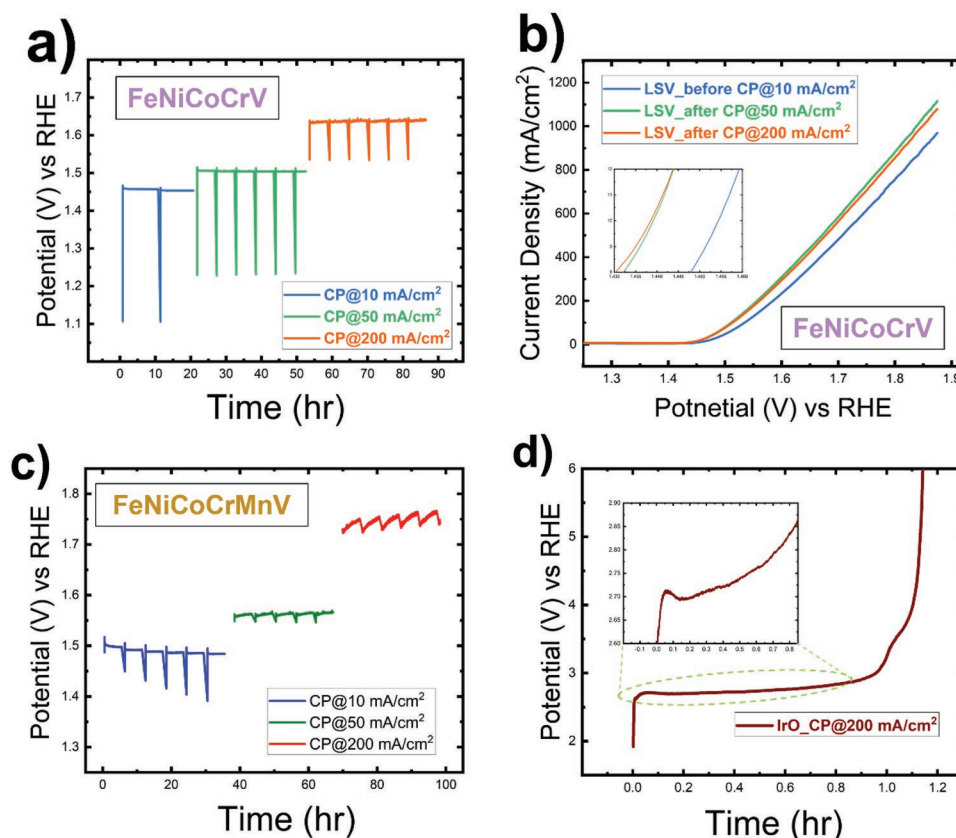electrocatalytic activity toward OER. Hg/HgO electrode with a plastic housing was selected as the reference electrode to ensure high stability and rigorous measurements at high pH values. Commonly observed literature and as will be discussed in later sections, nanoparticles oxidize under OER reaction condition. The measurements were conducted in N_2-saturated 1 M KOH electrolyte. N_2 was bubbled into the electrolyte for at least 45 min to ensure a complete deaeration of the electrolyte medium from any oxygen species prior to OER activity measurements. After activating the catalyst by performing five cyclic voltammetry (CV) scans, OER activity was probed by performing linear sweep voltammetry (LSV) at 5 mV s^{-1} scan rate. The overpotential at 10 mA cm^{-2} is the characteristic metric used herein to evaluate the performance of HEO catalysts. Fe, Ni, and Co have been shown in the literature to possess high OER activity. Therefore, ternary FeNiCo HEO was selected to be the benchmark catalyst, to which the alloying effects of Cr, Mn, and V are further evaluated. Results showed that the addition of either Cr, Mn, or V boosted the activity of their respective quaternary-HEO

catalysts compared to ternary-HEO FeNiCo catalyst. OER activity ranking is FeNiCoCr > FeNiCoMn > FeNiCoV > FeNiCo, with overpotentials calculated to be 240, 262, 274, and 291 mV, respectively, as shown in **Figure 3**a. The alloying order was then further increased to quinary. Mixing of Cr and V to make FeNiCoCrV quinary-HEO catalyst showed a dramatic enhancement in OER activity with a lower overpotential of 220 mV. FeNiCoCrMn showed higher activity than quaternary FeNiCoMn, but lower than FeNiCoCr, as shown in Figure 3c. This could be due to lower Mn concentration, as shown by EDX analysis. Increasing the alloying order from quaternary (FeNiCoMn and FeNiCoV) to quinary (FeNiCoMnV) showed enhancement in OER activity. Nevertheless, FeNiCoMnV quinary-HEO still shows slightly lower OER performance than FeNiCoCr quaternary-HEO. This implies that the nature of the alloying element itself (i.e., Cr) possesses a higher importance in dictating the OER activity, compared to the alloying order (i.e., quinary vs quaternary). Reduction of performance while increasing the alloying order could be a result of the decrease in the number
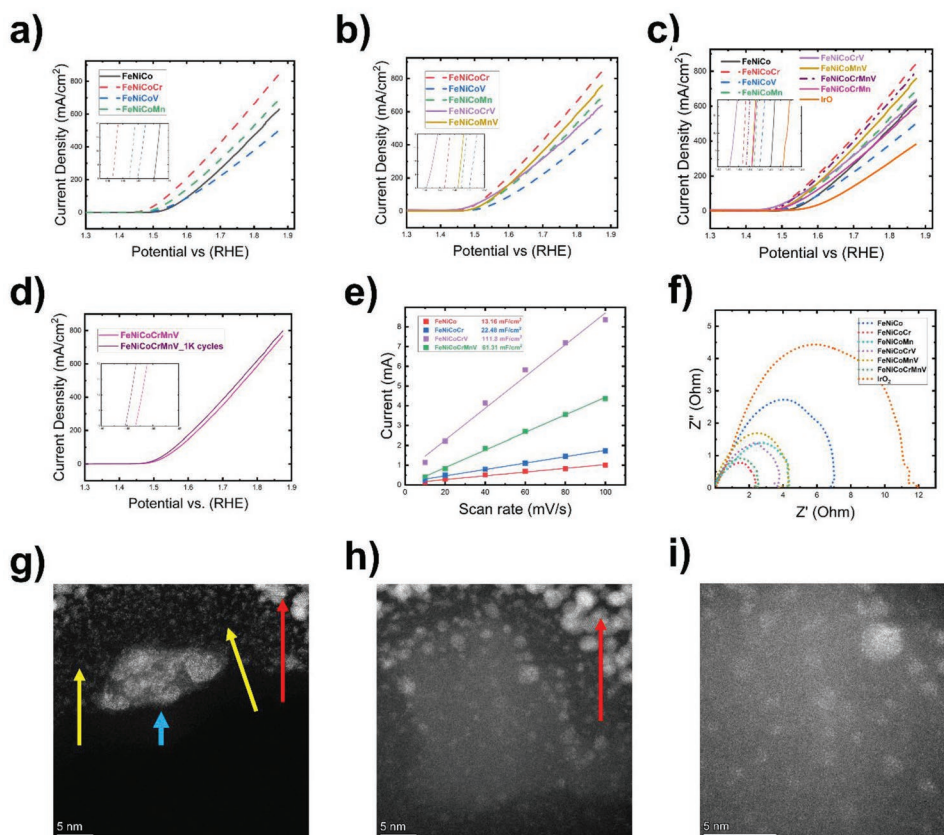
Figure 3. LSV scans for HEO-catalysts synthesized on carbon fiber paper GDL, tested in N_2-saturated 1 M KOH. All potentials reported versus RHE reference electrode. a) LSV scans comparing the effect of introducing either Cr, V, or Mn to FeNiCo to form quaternary-HEO catalyst. b) LSV scans comparing the performance of quaternary-HEO and quinary-HEO catalysts, shown as dashed and solid lines, respectively. c) LSV scans showing the performance of different HEO-catalysts with sequential alloying orders (quaternary, quinary, and senary) in comparison to state-of-the-art IrO$_2$ catalyst. d) LSV scans showing the performance of FeNiCoCrMnV senary-HEO catalyst before and after 1000 ADT cycles, in pink and purple, respectively. All insets (a–d) are zoomed-in to show the trend of overpotential at 10 mA cm^{-2}, with potentials reported at x-axis versus RHE reference electrode. e) ECSA deduced from double-layer capacitance at different scan rates shown at x-axis and current represented at y-axis. f) EIS Nyquist plots show significantly higher resistance for IrO$_2$ catalyst compared to HEO catalysts. g) STEM image for FeNiCoCrMnV after OER testing, showing a set of small nanoparticles aggregate (indicated by blue arrow), in addition to a sea of single-atom catalysts (indicated by yellow arrows). Red arrow in (g,h) points toward Pt protection layers, used during FIB cross-sectioning. h,i) STEM image showing an abundance of nanoparticles with 1–2 nm size and others of few clusters of atoms.

**ADVANCED
SCIENCE NEWS**

www.advancedsciencenews.com

**ADVANCED
ENERGY
MATERIALS**

www.advenergymat.de

Figure 4. a) Chronopotentiometry (CP) analysis of FeNiCoCrV sample. The sample was tested at constant current densities of 10, 50, and 200 mA cm^{-2}, shown in blue, green, and orange, respectively. CP at any given current density was performed in cycles. Each cycle consisted of a CP for 5 h, followed by OCV for 30 min. b) LSV scans recorded at 5 mV s^{-1} measured before ADT, after completion of CP^{50} and CP^{200}, shown in blue, green, and orange, respectively. c) CP analysis of FeNiCoCrMnV sample, at similar protocol as (a). d) CP^{200} for IrO$_2$ catalyst.

of catalytically active sites. Considering Co and Ni to be the active sites, their total concentrations in a quaternary-HEO (e.g., FeNiCoV) is 50%, compared to 40% in a quinary-HEO (e.g., FeNiCoCrV). Therefore, active sites concentration does not seem to explain our results, as quinary FeNiCoCrV (with less Co and Ni) showed higher activity compared to quaternary FeNiCoCr and FeNiCoV. On the other hand, the addition of certain elements (e.g., Cr, Mn, or V) to FeNiCo may affect the oxidation state of the Fe, Ni, and/or Co. The development of higher valence states has shown some positive effect on the OER activity (e.g., Co^{4+} has higher OER activity than Co^{3+} or Co^{2+}).[49–52] For comparison, IrO$_2$ commercial catalyst had an overpotential of 320 mV at 10 mA cm^{-2}, 100 mV worse than FeNiCoCrV samples measured under the same testing conditions.

Senary-HEO composed of FeNiCoCrMnV showed intermediate enhancement in performance with an overpotential of 247 mV at 10 mA cm^{-2}. **Figure 4**d shows the performance of senary-HEO FeNiCoCrMnV catalyst after being tested for 1000 cycles. Performing 1000 CV showed an enhancement in OER activity, where overpotential was further improved by 8 mV at 10 mA cm^{-2}. The performance enhancement during cycling could be attributed to surface restructuring or due to the leaching of some less-stable elements from the HEO catalyst (i.e., dealloying). Dealloying of Mn, Cr, or V may lead to maximizing the presence of other active elements (i.e., Fe, Ni, or Co)

at the catalyst surface or increasing the electrochemical active surface area (ECSA).[53,54] Another hypothesis suggests that the increase in OER activity, with dealloying, may occur when some elements (e.g., Mn) redistribute to the surface before leaching out into the electrolyte. The presence of Mn with a higher population in the vicinity of Ni or Co, at the sample surface, was reported to increase the catalytic activity due to facile deprotonation of OH$^-$.[55]

ECSA was deduced from double-layer capacitance obtained by performing CV sweeps at different scan rates: 10, 20, 40, 60, 80, and 100 mV s^{-1}, as shown in Figure 3e. Results showed that FeNiCo catalyst has the smallest ECSA with 13.16 mF cm^{-2}. FeNiCoCrV HEO catalyst possesses an order of magnitude larger ECSA of 111.8 mF cm^{-2}, compared to ternary FeNiCo catalyst. ECSA data agree with OER analyses derived from LSV scans in Figure 3a–c. On the contrary, FeNiCoCr obtained an ECSA of 22.48 mF cm^{-2}, which is approximately fivefolds smaller than FeNiCoCrV quinary HEO catalyst. Electrochemical impedance spectroscopy (EIS) was performed at 1.6 V versus RHE, after OER onset occurred for all the catalyst, as shown in Figure 3f. EIS showed a higher impedance for IrO$_2$ catalyst compared to HEO non-noble metal catalysts. Incorporation of Cr, Mn, and/or V into FeNiCo showed a reduction of HEO impedance, which agrees with the trend of enhancement in OER activity. FeNiCoCr showed the smallest impedance at

**ADVANCED
SCIENCE NEWS**
www.advancedsciencenews.com

**ADVANCED
ENERGY
MATERIALS**
www.advenergymat.de

1.6 V, followed by FeNiCoCrMnV and FeNiCoCrV, which follows the same trend from LSV sweeps in Figure 3c. This further aligns with the observation that the addition of Cr has the biggest impact on increasing the OER activity, compared to Mn or V. Tafel slope analysis was carried out over a long potential range of 100 points to ensure a higher level of accuracy of the data analyzed. In general, HEO catalyst showed an average of twofolds shallower slope than IrO_2 commercial catalyst, with the latter having a slope of ≈90 mV dec^{-1}. The shallower slope of HEO catalyst indicates faster charge transfer for HEO catalysts than IrO_2, which further explains their superb OER activity. Synthesized HEO catalysts did not show a very significant difference relative to one another in terms of Tafel slope values (45–58 mV dec^{-1}). This could still fall within the marginal errors during sample testing or data processing during linear regression fitting. Tafel slope analyses for different catalysts are presented in Figures S6–S11, Supporting Information.

STEM analysis for the same HEO catalyst (i.e., FeNiCoCrMnV) was carried out after OER testing (but before any long-stability testing). The morphology of the sample was significantly different than the pristine sample (i.e., before OER testing). After OER, HEO catalysts' morphology is composed of significantly smaller nanoparticles, never observed before OER testing. Figure 3g shows a set of smaller nanoparticles. The appearance of smaller nanoparticles observed by STEM after sample testing for OER could occur under multiple scenarios. One possibility suggests further particle fission takes place at RT, driven by electrochemical reaction. As described earlier, the synthesis mechanism of HEO NPs in CTS thermochemical shock involves scavenging oxygen from carbon support to react with dissolved carbon. With OER operation, an abundance of oxygen is generated near the catalyst and carbon support, where carbon's surface oxidizes (i.e., becoming rich of oxygen). Hence, with high operating voltage and oxygen abundance, HEO NPs experience the necessary driving forces for particles to split (i.e., fission) and form smaller particles, by "RT electrochemical shock." A recent in situ TEM study at 300 °C showed peristalsis-like migration of catalytically active Pd nanoparticles and their splitting when oxygen gas is presented along with carbon-rich environment at the particle vicinity.[38] Microscopic imaging showed a dependence of the particle migration and fission on the abundance of oxygen and carbon, where the depletion of any of them results in reduced fission and eventually Ostwald ripening. A second scenario may proceed as under OER conditions (cycling to positive potentials in highly corrosive pH environment), particles became porous due to gas bubbles punching. Similar observation has been reported in literature where metal nanoparticles became porous under OER condition.[40] This increased the structures' porosity and ECSA in return. Both mechanisms of morphology perturbation after OER may happen simultaneously, of course with different energetics, where one is more favorable than the other. Further complementary and more detailed studies, beyond the scope of the current study, are highly encouraged to unravel the exact reformation mechanism.

Moreover, an abundance of single-atom catalysts (SAC) emerged after OER, as shown in Figure 3g–i is and other larger particles. SAC may generate from the adsorption of the pre-dissolved elements (e.g., Cr, V, and Mn) from HEO nanoparticles. This claim may be valid given the fact that significant carbon defects and dangling bonds exist due to carbon oxidation under OER conditions.[13,56] XPS analysis confirmed the significant oxidation of carbon (Figure S19, Supporting Information). It is worth mentioning that the red arrow, in Figure 3g,h, is pointing toward Pt nanoparticles, which is from a thin layer of Pt used as protection during TEM cross-sectioning of the sample with focused ion beam (FIB). Figure 3h,i shows very tiny nanoparticles (1–2 nm in diameter). This observation is in line with other literature reports, where catalyst morphological perturbations occur at catalyst surfaces during OER (e.g., increased surface roughness and porosity).[40,41,47] In addition, recent literature report showed that surface reconstruction for HEO system can happen under electrochemical activation or during OER.[23,57–59] All our synthesized HEO catalysts, regardless of their alloying order (ternary, quaternary, quinary, or senary), showed a significantly higher OER activity compared to state-of-the-art commercial IrO_2 catalyst. More detailed investigations of the catalyst's stability and the mechanism behind the activity enhancement will be discussed in the following sections.

2.3. Accelerated Durability Testing

Catalyst stability is a crucial factor in ensuring longevity under operating conditions for extended hours with a reasonable performance. A major challenge, in addition to the poor activity and high cost of IrO_2 catalyst, is its limited lifetime, which adds a burden to AEMEC technology commercialization. Therefore, designing a stable catalyst is highly desirable. HEO catalyst stability was investigated under constant current mode (i.e., chronopotentiometry (CP)), while observing the potential simultaneously. Samples were tested at constant currents of 10, 50, and 200 mA cm^{-2}, denoted as CP^{10}, CP^{50}, and CP^{200}, respectively. FeNiCoCrV sample was tested successively for 20, 35, and 35 h at CP^{10}, CP^{50}, and CP^{200}, respectively (90 h total). Each CP step was carried out in intervals of 5 h. The sample was kept at OCV for 30 min to relieve the gas bubbles accumulating on the catalyst surface, which form due to piecewise constant applied current, between each CP step.[60] Holding the catalyst at OCV refreshes the catalyst surface for the next cycles of CP testing. After each set of CP^{10}, CP^{50}, and CP^{200}, LSV was performed at 5 mV s^{-1} to observe the actual degradation in performance (i.e., increase in overpotential). FeNiCoCrV samples, as shown in Figure 4a, showed highly robust and stable performance. During CP^{10}, potential change over 20 h was negative (i.e., the potential value dropping instead of increasing), which indicates a reduction in overpotential and enhancement in OER activity, as shown in Figure S12, Supporting Information. The accumulated overpotential drop after 20 h was 6 mV. The same behavior was observed for CP^{50} for 35 h, and the potential dropped by an additional 5 mV. During CP^{200}, overpotential shifted positively by 8 mV. The rate of potential change for CP^{10}, CP^{50}, and CP^{200} is −0.4, −0.14, and 0.228 mV h^{-1}, respectively. Overall, after 90 h of CP testing at different current densities, potential change was in favor of enhancing OER activity (i.e., lower overpotential), instead of increasing as commonly cited in the literature. The overpotential after 90 h of testing at higher current densities was 208 mV. Figure 4b shows LSV scans recorded before ADT

starts, after CP^{50} and CP^{200}. The results showed an enhancement in the current density and overpotential compared to the LSV recorded before testing, with an overpotential reduction at 10 mA cm^{-2} by 16 mV. The aforementioned observation shows evidence of the great stability demonstrated by our FeNiCoCrV catalyst, without any decay in the performance.
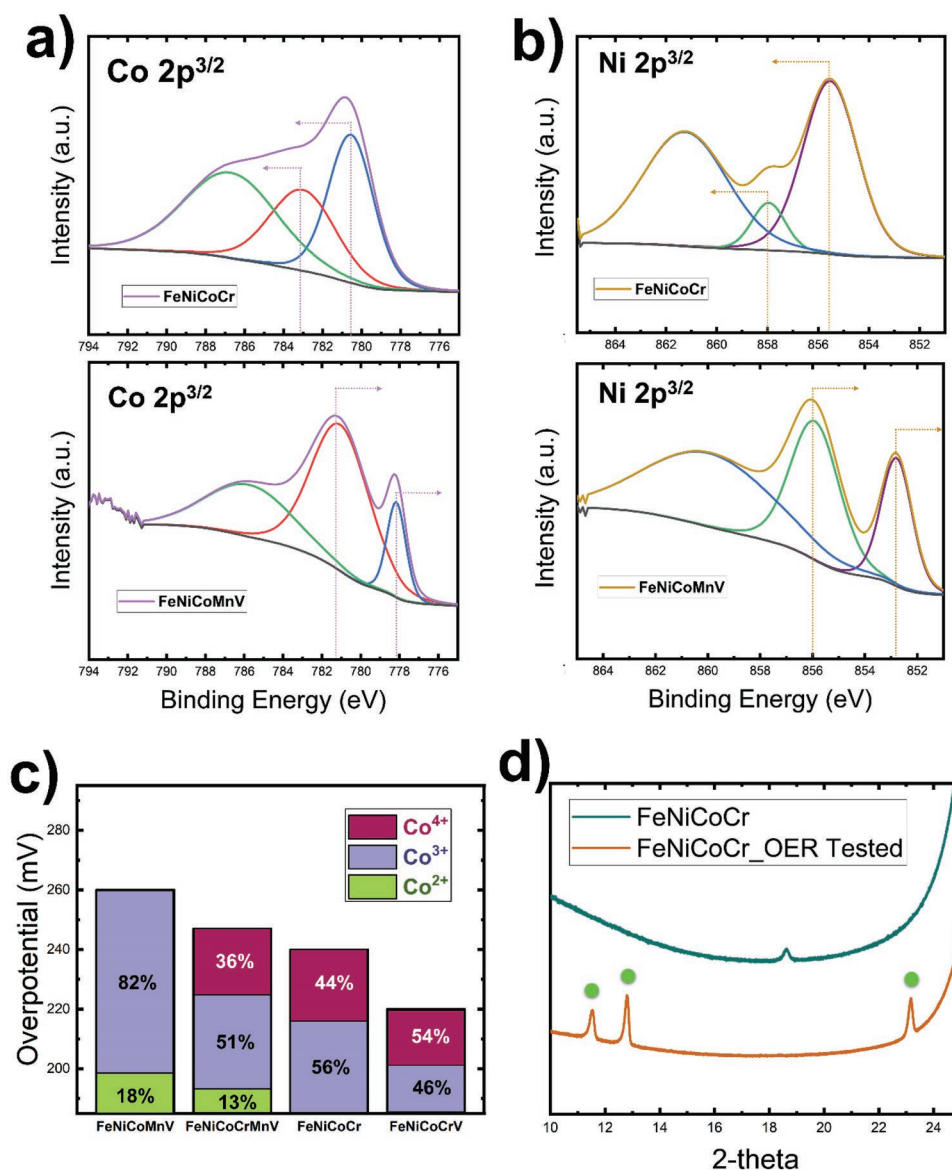
Catalyst stability of FeNiCoCrMnV was tested following the same protocol for FeNiCoCrV counterpart, as shown in Figure 4c. At lower current densities CP^{10}, the sample showed similar behavior with a negative shift of potential, indicating an enhancement in OER activity. On the contrary, at higher current densities (i.e., CP^{200}), the potential increase during each interval (i.e., before holding the sample at OCV) was significant, by 3 mV h^{-1}. Nevertheless, after OCV was applied for 30 min, the potential dropped significantly. This implies that samples containing Mn (e.g., FeNiCoCrMnV) possessed a higher binding affinity with reaction intermediates/products. State-of-the-art IrO_2 catalyst was tested under the same conditions for CP^{200}. IrO_2 showed a spontaneous rise in potential from 1.79 to $\approx$2.72 V, as shown in Figure 4d, after which potential stabilizes around 2.7 V for less than 1 h, before an exponential potential jump is observed. Potential jump to high voltages is considered a total deactivation of the catalyst, resembling the end of the catalyst lifetime.[61,62] The lowest-performing catalyst of the synthesized HEO herein (i.e., FeNiCo) was tested under similar conditions to IrO at CP^{200}, under constant mode without any OCV relief setup, as shown in Figure S15, Supporting Information. Results showed that FeNiCo HEO was stable for up to 45 h at CP^{200}, without observing any potential jumps. The profile of potential change was almost flat, with an overall potential increase rate of $\approx$0.97 mV h^{-1}. The presented results of HEO catalysts, developed following a high-throughput approach, showed two orders of magnitude higher stability than the IrO_2 catalyst without noticeable decay in OER performance. Combining the high activity and tremendous stability renders our noble-metal-free HEO catalyst as a candidate to replace noble metal IrO_2 catalyst.

3. Origin of OER Activity and Stability Enhancement

Typically for non-precious metal catalysts, the transition metal (e.g., Co, Ni, or Fe) is the active species for electrocatalysis. Hence the activity of the transition metal center is highly dependent on the metal-oxygen covalency (i.e., strong, or weak interaction). The strong interaction between metal and oxygen is a function of metals' oxidation state. Increasing the oxidation state means an increase in the transition metal electronegativity, and a reduction of the 3d orbital filling (i.e., fewer number of electrons occupying 3d orbitals). Thus, more overlapping between 3d and 2p orbitals from metals and oxygen, respectively, is expected, where the Fermi level is shifting downward. In consequence, metal-oxygen hybridization is more dominant and OER energy penalty (i.e., overpotential) is decreased.[63,64] For example, $LiCoO_2$ was found to possess higher OER activity when delithiation took place, which resulted in increasing the oxidation state of the Co atom (i.e., increasing ratio of Co^{4+} to Co^{3+}), promoting more oxygen-metal orbitals hybridization.[65]

Similar observations have been shown for different structures (e.g., perovskite and spinel oxides), and for other metal centers, including Ni and Fe.[55,63,66] In the same context, a prominent strategy is TM alloying, which improves the electrocatalytic activity due to synergistic effects induced on the active elements (e.g., Co, Ni, and/or Fe for OER) by modulating their electronic configurations and oxidation states.[23,49,51,55] Molin et al. showed, for FeNiCo trimetallic alloy, varying the alloying percentage affects the oxidation state, which affected their OER performance in return.[67] Iron alloying with Co showed enhancement of OER activity, comparable to those of Ni-Fe benchmark catalysts. Fine-tuning of Fe-Co alloying ratio showed that at ratios where Fe oxidation state increases (i.e., formation of Fe^{4+} over Fe^{3+}), the catalytic activity of the Co center is significantly enhanced, as well as that of Fe.[51] A similar observation has been shown for Ni center alloyed with Fe, when Fe oxidation state increases.[68] Moreover, several studies showed that Co^{4+} presence enhances the OER activity.[69,70] Co^{4+} possesses higher electronegativity compared to lower oxidation states (i.e., Co^{3+} and Co^{2+}), which facilitates the formation of -OOH reaction intermediate due to enhanced electrophilic interaction between Co^{4+} and surface-adsorbed oxygen species. In summary, increasing the oxidation state of Co, Ni, and/or Fe has been shown to improve their OER catalytic activity.

X-ray photoelectron spectroscopy (XPS) analysis of $2p^{3/2}$ photoemissions of Co and Ni are shown in **Figure 5**a,b, respectively. The top panels represent the photoemissions of FeNiCoCr, while the bottom panels represent data of FeNiCoMnV, to elucidate the difference of addition Cr versus Mn and V, and their influence on the electronic configuration of Co and Ni. Cr incorporation into FeNiCo showed a significant effect on the electronic configuration of Co by promoting the formation of higher oxidation states for Co (i.e., Co^{4+} and Co^{3+}), which is shown by a significant shift of $2p^{3/2}$ peaks to higher binding energies by $\approx$1.5 eV. Meanwhile, Co $2p^{3/2}$ of FeNiCoMnV sample was located at lower binding energies. A similar observation is shown in Figure 5b for Ni $2p^{3/2}$ photoemissions. Ni $2p^{3/2}$ of FeNiCoCr was shifted to higher binding energies, implying an increase in the Ni oxidation state. On the other hand, samples including Mn and V (i.e., FeNiCoMnV) had their XPS Ni $2p^{3/2}$ positioned at lower binding energies compared to those of FeNiCoCr counterparts. Figure 5c shows a direct comparison of different Co oxidation states in correlation to OER overpotential. XPS peak deconvolution was performed for all the samples to quantify the percentages of different Co oxidation states (Co^{2+}, Co^{3+}, and Co^{4+}) for each sample. FeNiCoMnV sample obtained an overpotential of 260 mV, while peak deconvolution of Co $2p^{3/2}$ showed the presence of Co^{3+} and Co^{2+} with 82% and 12%, respectively. FeNiCoCrMnV obtained a 247 mV overpotential, while showing the presence of all three oxidation states of Co^{2+}, Co^{3+}, and Co^{4+}, of 13%, 51%, and 36%, respectively. The top-performing FeNiCoCrV sample showed an overpotential of 220 mV, in correlation with the maximum percentage of Co^{4+} species. In addition to the aforementioned observation, according to Li et al., increasing the oxidation state of Fe from Fe^{3+} to Fe^{4+} enhances the activity of Co active center.[51] XPS analysis showed an increase in Fe oxidation state for FeNiCoCr sample compared to that of FeNiCoMnV counterparts, as shown in Figure S17, Supporting Information.

**ADVANCED
SCIENCE NEWS**

www.advancedsciencenews.com

**ADVANCED
ENERGY
MATERIALS**

www.advenergymat.de

Figure 5. a,b) XPS spectra of Co 2p$^{3/2}$ (left) and Ni 2p$^{3/2}$ (right) for FeNiCoCr and FeNiCoMnV, top and bottom, respectively. XPS spectra of FeNiCoCr shifted to higher BE compared to those of FeNiCoMnV. c) Bar chart showing the correlation between OER overpotential and quantified the percentage of Co oxidation state species for each sample set of FeNICoMnV, FeNiCoCrMnV, FeNiCoCr, and FeNiCoCrV. d) Cropped XRD spectra of FeNiCoCr before OER testing (i.e., pristine) and after OER ADT testing showing an emergence of new peaks belonging to the oxyhydroxide phase, highlighted with green circles.

Fe-Co spinel compounds, reported in the literature, have shown a tendency toward the formation of oxyhydroxide phase during testing under OER conditions in aqueous alkaline medium.[41,47] Cycling the samples under OER conditions results in increasing the oxidation state of Co species and surface reconstruction was observed, where more porosity evolved.[40,41,47] These observations aligned with our STEM imaging analysis, as shown in Figure 3. Therefore, XRD measurement was performed to unravel the structural changes that occurred after testing HEO catalyst in OER. XRD analysis for samples post OER testing showed the emergence of several new peaks, which implies the formation of new phases. New peaks located at 11.5°, 13°, and 23° 2θ angles are attributed to

oxyhydroxide phases.[43,44] Oxyhydroxide phases are reported in the literature to resemble the benchmark activity toward OER. Therefore, the dynamic reconstruction of our HEO to obtain oxyhydroxide phase under OER may be a keystone to boosting their catalytic activity.

XRD analysis for the post-OER samples showed several additional peaks emerging in the region between 30° and 55° 2θ (inset in **Figure 6**a). Pristine carbon fiber support (i.e., without any metal deposition) was tested following the same OER protocol. XRD analysis was performed after OER testing on the pristine carbon fiber. No change in the carbon peaks spectrum was noticed, as shown in Figure S16, Supporting Information. Therefore, the emergence of the additional peaks
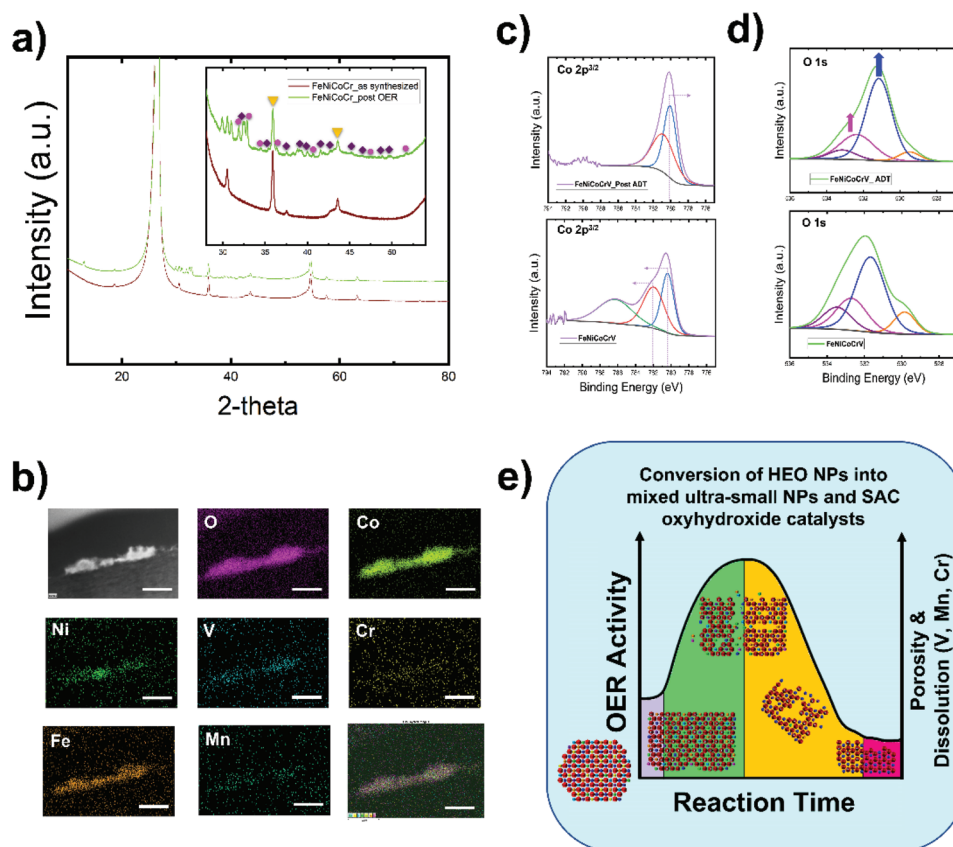
Figure 6. a) XRD spectra of FeNiCoCr showing emergence of carbide phase (denoted by purple diamond), in addition to original spinel phase and newly developed oxyhydroxide phases, denoted by yellow triangle and pink circle, respectively. b) EDX mapping for FeNiCoCrMnV, obtained from TEM imaging of a single particle (top left panel) post-ADT for 100 h, with a scale bar of 100 nm. c,d) XPS spectra of O 1 s (right) and Co 2p3/2 (left) for FeNiCoCrV before and post ADT, bottom and top, respectively. After prolonged ADT testing, Co 2p3/2 showed a shift to lower BE, with the disappearance of satellite peak. XPS of O 1 s showing an increase in signal obtained for highly oxygenated species (O^{2-}/O^{-}) and surface adsorbed $-OH/O_2$, shown in blue and magenta, respectively, after ADT for 75 h. e) Cartoon showing the evolution of HEO structure as a function of time and its corresponding OER performance. Fe, Ni, and Co in spinel structure shown as hard spheres in blue, while turning brown in oxyhydroxide phase. Cr, Mn, and V are shown in green, orange, and fuchsia. Initially, HEO convert from oxide to oxyhydroxide active phase. In addition, sample porosity increases under OER processing, where sub-nanoparticles and single atom catalyst evolve. Dissolution of less stable elements (i.e., Mn, V, and Cr) lead to further increase in OER activity due to enlarged ECSA and more favorable deprotonation of reaction intermediates. Complete loss of alloying elements takes place along the course of accelerated durability testing, where OER activity diminishes due to losing the alloying synergistic and shrinking of ECSA.

(30–55° 2θ) is believed to be due to the formation of crystalline carbide phases of HEO NPs, in addition to the oxyhydroxide phases. Transition metal carbides have shown interesting electrocatalytic activity and stability toward OER in alkaline solution.[71,72] In addition, transition metal carbides, when used as a support in a core@shell catalyst architecture, showed enhanced stability in addition to boosting the OER catalytic activity.[39] Furthermore, the electronic conductance of the catalyst system is a key factor. Boosting the electrical conductance of transition metal catalyst systems has been of great interest in literature, where introducing oxygen vacancies or dual heteroatom doping (e.g., forming oxy-nitride phase) were deemed to be prominent strategies.[1,10,49,73] In the same context, the significantly higher electronic conductivity of metal-carbide phases compared to metal oxide phases may be a key factor in boosting the OER activity of HEO NPs. The coexistence of the newly developed oxyhydroxide and carbide phases, in addition to the dominant spinel oxide phase suggests that the new phases are formed at the utmost layers of the surface of HEO NPs. The peak intensity

ratio, deduced from XRD spectra, of the most dominant peak of spinel oxide/oxyhydroxide/carbide phases is 14/4.5/6, respectively. Oxyhydroxide phases are activated with direct interaction between HEO and alkaline electrolyte medium under reaction conditions. Carbide phases are formed due to reconstruction of the carbon atoms at the interface between HEO nanoparticles and carbon fiber support. Enhanced electronic conductivity of the carbide phases and the strong nature of metal carbide phases are two major factors to boost OER activity and stability, respectively. The existence of HEO-carbide bonds is believed to enhance the mechanical stability of the catalyst system against gas bubbles evolution during OER, where high capillary forces may pull off catalysts from GDL (erosion).[39]

Aside from the formation of strong carbide intimacy between HEO and carbon support, which mechanically stabilize the NPs, the chemistry of the nanoparticle plays a major role in influencing its stability. Layered nickel hydroxide structures showed higher stability and activity in an alkaline medium with proper substitution of Ni with other elements (i.e., Co

or Mn).[55] Ni substitution with Co and/or Mn decreased the deprotonation energy, which can help boost the OER activity. DFT calculation suggested that hydrogen favors the desorption at or near the substituted elements (i.e., Mn or Co) due to facile electron transfer.[55] As observed earlier in the presented data herein, as shown in Figures 3d,4a,b, OER activity was enhanced instead of degrading during ADT testing. Therefore, XPS, ICP, and STEM/EDX analyses are key to unraveling the surface composition changes during ADT and its correlation to OER performance.

Inductively coupled plasma mass spectrometry (ICP-MS) was used to discover the change in elemental composition after ADT for 90 h. ICP results showed significant loss of Cr compared to Fe, Ni, or Co, as shown in Figure S5, Supporting Information. Cr loading dropped by 43% after ADT testing for 90 h, following a similar protocol as shown in previous sections. In addition, Co and Ni loading were also reduced, however, with smaller ratios compared to Cr. This infers that Fe, Ni, and Co have higher stability compared to Cr, V, and Mn, which can easily leach out from HEO NPs (i.e., evolve faster from bulk to the surface). In this context, three factors may exist and be the reason for OER enhancement: i) with the leaching of Cr, Mn, and V during OER, more active sites became available at the surface (e.g., Fe, Ni, or Co), where more reaction intermediates can be bound. ii) the less stable elements (e.g., Mn, Cr, or V) evolve to the surface where their presence in the vicinity of the other catalytically active sites (Fe, Ni, or Co) may induce further changes on the oxidation states of the later (i.e., increasing the oxidation states of the latter). iii) In addition, the presence of Mn, Cr, or V at the surface may reduce the deprotonation energy and act as a favorable site for hydrogen desorption.[55,74]

To validate these hypotheses, ex situ XPS analysis was performed for samples during ADT, which showed intensified Mn signal after operating for 1000 cycles, as shown in the Figure S18, Supporting Information. This provides an additional confirmation that during OER less stable alloying elements (i.e., Mn, and similarly Cr or V) evolve from the bulk toward the surface (i.e., dealloying). Mn presence at the surface vicinity with Co and Ni can stimulate easier deprotonation of OH^- to occur.[55] EDX mapping obtained from TEM imaging of FeNiCoCrMnV after extended ADT testing, as shown in Figure 6b, provides further insights into the elemental stability and distribution uniformity. Co, Fe, and Ni signals remained intense across the particle morphology. However, Ni mapping showed a slight concentration away from Co (i.e., phase segregation). Fe showed an even random distribution across the particle. This observation agrees with ICP-MS analysis, where Fe showed the least dissolution rate, followed by Ni and Co. Lower intensity signals were detected for V, Cr, and Mn, which implies lower stability for those elements with a higher tendency to dealloying during prolonged and under harsh ADT conditions.

Moreover, further extended ADT testing was performed, and Figure 6c shows XPS spectra of Co $2p^{3/2}$ for FeNiCoCr after prolonged ADT. Hence, Co $2p^{3/2}$ peak was significantly shifted to lower binding energies, with dominant Co^{2+}/Co^0 species. The later analyses suggest that during OER Cr, Mn, and V atoms evolve to the surface. Their evolution to the surface did not show an immediate negative effect on OER but instead further enhanced the performance of our HEOs catalysts' activity. With

prolonged testing and the total dissolution of those less-stable elements, the structure was reduced to FeNiCo with a lower oxidation state and lower OER activity.

Figure 6d shows O 1 s XPS spectra for FeNiCoCr samples before and during ADT. O 1 s peak deconvolution showed the presence of 4 sub-peaks. Peaks located at 529.45, 531.2, 532.3, and 533.05 eV are ascribed to lattice oxygen, adsorbed highly oxidative species (O_2^{2-}/O^-), surface adsorbed O_2/-OH, and surface adsorbed H_2O, respectively. Highly oxidative species (O_2^{2-}/O^-) have been reported to form in alkaline solutions and are highly active toward OER.[50,75] In addition, the presence of surface adsorbed O_2/-OH can indicate qualitatively the availability of catalytic active sites for OER. The activity was in fact further enhanced. Peak area analysis of the deconvoluted O 1 s spectra, in Figure 6a, showed an increase in the relative peak area ascribed to highly oxidative species (O_2^{2-}/O^-) from 51.5% to 62% after ADT started. The same observation was cited for peak area change of surface adsorbed O_2/-OH to increase from 22.7% to 25% after ADT started. This observation aligns with the enhancement of OER performance during ADT, as observed in Figure 4.

In summary, based on data analysis, synthesized HEO catalyst maintained a spinel oxide structure. Right under OER testing conditions, structure changes to maintain an oxyhydroxide phase, represented by a cartoon in Figure 6d, by changing the active elements color (i.e., Fe, Ni, and Co) from blue to brown. In addition, particles' morphology changes from large nanoparticles, into mixed ultra-small nanoparticles (1–2 nm) and SACs, as shown in Figure 6d, transition from lavender to green shaded area. According to ICP and EDX analysis, tendency to dissolution of Cr, Mn, and V are much larger than Fe, Ni, and Co. Thus, under ADT testing, less stable Cr, Mn, and V (shown in green, orange, and fuchsia) evolve more from the bulk into the surface, increasing the OER activity. OER activity is anticipated to reach a maximum value, after which activity starts to degrade until a complete dissolution of Mn, V, and Cr occurs, as shown by structural transition into the orange region. With further extended ADT testing, dissolution of Fe, Ni, and Co has a dominant effect, until reaching a complete catalyst deactivation that happens with degradation of ECSA, as shown in the fuchsia region of Figure 6d. Dynamic reconstruction of the catalyst structure under reaction conditions yielded the formation of a very strong chemical bond between HEO and carbon fiber (i.e., metal-carbide). This further enhanced the HEO stability to surpass that of IrO_2 catalyst by two orders of magnitude.

Alloying has been proven to be a vital strategy to enhance OER activity, while some elements have shown more positive effects (e.g., Cr and V) than others (e.g., Mn). Further exploration of different alloying ratios (i.e., $Fe_xNi_yCo_zCr_dMn_{1-x-y-z-d}$) might be useful to develop a highly active catalyst with significant longevity, where the onset of the complete dissolution of less stable elements is well extended beyond the desired lifetime of AEMEC OER catalyst.

4. Conclusion

The presented study provided significant insights into the role of different alloying elements. Results showed that Cr, Mn, and

V additions boosted the OER activity, whereas Cr showed higher influence on the oxidation state of Fe, Ni, and Co active sites. Cr addition boosted OER activity by the promotion of higher oxidation states of active elements (Co, Ni, and Fe). In addition, Cr addition contributed to maximizing the amount of adsorbed highly oxidative species and surface oxygen species (O_2/OH$^-$). Tremendous stability was observed for non-noble metals HEO, where under higher current densities, no performance decay was noticed. Stability originated from strong chemical intimacy achieved by forming strong metal-carbide bonds between HEO nanoparticles and carbon from the substrate. Non-noble metal HEO showed two orders of magnitude higher stability compared to state-of-the-art IrO_2 catalyst, and smaller overpotential, as well. During ADT, samples showed a higher activity at the beginning due to morphological reconstruction into smaller particles and single atom catalysts, during evolution of less stable Mn and Cr from the bulk to the surface. After prolonged ADT testing and with total dissolution of Cr, OER catalytic activity was deteriorated due to subtle reduction in the oxidation states of active species. Therefore, further detailed investigations of different alloying ratios are encouraged to design an optimized catalyst with higher activity, meeting the desired operation lifetime.

Conflict of Interest

The authors declare no conflict of interest.

Data Availability Statement

The data that support the findings of this study are available from the corresponding author upon reasonable request.

[1] K. E. Salem, A. M. Mokhtar, A. Abdelhafiz, N. K. Allam, *ACS Appl. Nano Mater.* **2020**, *3*, 6078.

[2] Z. Chen, J. Shi, Y. Li, B. Ma, X. Yan, M. Liu, H. Jin, D. Li, D. Jing, L. Guo, *Energy Convers. Manage.* **2021**, *246*, 114668.

[3] T. N. Veziroglu, *Energy Procedia* **2012**, *29*, 654.

[4] A. Abdelhafiz, A. Vitale, C. Joiner, E. Vogel, F. M. Alamgir, *ACS Appl. Mater. Interfaces* **2015**, *7*, 6180.

[5] J. R. Varcoe, P. Atanassov, D. R. Dekel, A. M. Herring, M. A. Hickner, P. A. Kohl, A. R. Kucernak, W. E. Mustain, K. Nijmeijer, K. Scott, T. Xu, L. Zhuang, *Energy Environ. Sci.* **2014**, *7*, 3135.

[6] M. Bernt, A. Hartig-Weiß, M. F. Tovini, H. A. El-Sayed, C. Schramm, J. Schröter, C. Gebauer, H. A. Gasteiger, *Chem. Ing. Tech.* **2020**, *92*, 31.

[7] N. Ul Hassan, M. Mandal, G. Huang, H. A. Firouzjaie, P. A. Kohl, W. E. Mustain, *Adv. Energy Mater.* **2020**, *10*, 2001986.

[8] W. E. Mustain, P. A. Kohl, *Nat. Energy* **2020**, *5*, 359.

[9] N. Ul Hassan, M. Mandal, G. Huang, H. Adabi Firouzjaie, P. A. Kohl, W. E. Mustain, *Adv. Energy Mater.* **2020**, *10*, 2001986.

[10] K. E. Salem, A. A. Saleh, G. E. Khedr, B. S. Shaheen, N. K. Allam, *Energy Environ. Mater.* **2021**, https://doi.org/10.1002/EEM2.12324.

[11] M. P. Marceta Kaninski, V. M. Nikolic, G. S. Tasic, Z. L. Rakocevic, *Int. J. Hydrogen Energy* **2009**, *34*, 703.

[12] A. Vitale, H. Murad, A. Abdelhafiz, P. Buntin, F. M. Alamgir, *ACS Appl. Mater. Interfaces* **2019**, *11*, 1026.

[13] X. Ao, W. Zhang, B. Zhao, Y. Ding, G. Nam, L. Soule, A. Abdelhafiz, C. Wang, M. Liu, *Energy Environ. Sci.* **2020**, *13*, 3032.

[14] J. Song, Z. Xiao, Y. Jiang, A. A. Abdelhafiz, I. Chang, J. Zeng, *Int. J. Hydrogen Energy* **2019**, *44*, 11655.

[15] Y. Dong, I.-W. Chen, J. Li, *Chem. Mater.* **2022**, *34*, 5749.

[16] Z. Li, J. Song, D. C. Lee, A. Abdelhafiz, Z. Xiao, Z. Hou, S. Liao, B. DeGlee, M. Liu, J. Zeng, F. M. Alamgir, *Electrochim. Acta* **2020**, *329*, 135166.

[17] M. Bianchini, J. Wang, J. Wang, R. J. Clément, B. Ouyang, P. Xiao, D. Kitchaev, T. Shi, Y. Zhang, Y. Wang, H. Kim, M. Zhang, J. Bai, F. Wang, W. Sun, G. Ceder, *Nat. Mater.* **2020**, *19*, 1088.

[18] H. Peng, Y. Xie, Z. Xie, Y. Wu, W. Zhu, S. Liang, L. Wang, *J. Mater. Chem. A* **2020**, *8*, 18318.

[19] Y. Xin, S. Li, Y. Qian, W. Zhu, H. Yuan, P. Jiang, R. Guo, L. Wang, *ACS Catal.* **2020**, *10*, 11280.

[20] M. Cui, C. Yang, B. Li, Q. Dong, M. Wu, S. Hwang, H. Xie, X. Wang, G. Wang, L. Hu, M. Cui, C. Yang, Q. Dong, M. Wu, H. Xie, X. Wang, L. Hu, B. Li, G. Wang, S. Hwang, *Adv. Energy Mater* **2021**, *11*, 2002887.

[21] J. Cavin, A. Ahmadiparidari, L. Majidi, A. S. Thind, S. N. Misal, A. Prajapati, Z. Hemmat, S. Rastegar, A. Beukelman, M. R. Singh, K. A. Unocic, A. Salehi-Khojin, R. Mishra, *Adv. Mater.* **2021**, *33*, 2100347.

[22] T. Löffler, H. Meyer, A. Savan, P. Wilde, A. Garzón Manjón, Y.-T. Chen, E. Ventosa, C. Scheu, A. Ludwig, W. Schuhmann, T. Löffler, P. Wilde, Y. Chen, W. Schuhmann, H. Meyer, A. Savan, A. Ludwig, A. Garzón Manjón, C. Scheu, E. Ventosa, *Adv. Energy Mater.* **2018**, *8*, 1802269.

[23] N. Zhang, X. Feng, D. Rao, X. Deng, L. Cai, B. Qiu, R. Long, Y. Xiong, Y. Lu, Y. Chai, *Nat. Commun.* **2020**, *11*, 4066.

[24] S. D. Lacey, Q. Dong, Z. Huang, J. Luo, H. Xie, Z. Lin, D. J. Kirsch, V. Vattipalli, C. Povinelli, W. Fan, R. Shahbazian-Yassar, D. Wang, L. Hu, *Nano Lett.* **2019**, *19*, 5149.

[25] Z.-J. Chen, T. Zhang, X.-Y. Gao, Y.-J. Huang, X.-H. Qin, Y.-F. Wang, K. Zhao, X. Peng, C. Zhang, L. Liu, M.-H. Zeng, H.-B. Yu, *Adv. Mater.* **2021**, *33*, 2101845.

[26] S. Dou, J. Xu, X. Cui, W. Liu, Z. Zhang, Y. Deng, W. Hu, Y. Chen, *Adv. Energy Mater.* **2020**, *10*, 2001331.

[27] S. Liu, Z. Hu, Y. Wu, J. Zhang, Y. Zhang, B. Cui, C. Liu, S. Hu, N. Zhao, X. Han, A. Cao, Y. Chen, Y. Deng, W. Hu, *Adv. Mater.* **2020**, *32*, 2006034.

[28] C. Liu, Y. Shen, J. Zhang, G. Li, X. Zheng, X. Han, L. Xu, S. Zhu, Y. Chen, Y. Deng, W. Hu, *Adv. Energy Mater.* **2022**, *12*, 2103505.

[29] S. Liu, Y. Shen, Y. Zhang, B. Cui, S. Xi, J. Zhang, L. Xu, S. Zhu, Y. Chen, Y. Deng, W. Hu, *Adv. Mater.* **2022**, *34*, 2106973.

[30] Y. Chen, G. C. Egan, J. Wan, S. Zhu, R. J. Jacob, W. Zhou, J. Dai, Y. Wang, V. A. Danner, Y. Yao, K. Fu, Y. Wang, W. Bao, T. Li, M. R. Zachariah, L. Hu, *Nat. Commun.* **2016**, *7*, 12332.

[31] Y. Yao, Z. Huang, P. Xie, S. D. Lacey, R. J. Jacob, H. Xie, F. Chen, A. Nie, T. Pu, M. Rehwoldt, D. Yu, M. R. Zachariah, C. Wang, R. Shahbazian-Yassar, J. Li, L. Hu, *Science* **2018**, *359*, 1489.

[32] Y. Yao, Z. Huang, P. Xie, L. Wu, L. Ma, T. Li, Z. Pang, M. Jiao, Z. Liang, J. Gao, Y. He, D. J. Kline, M. R. Zachariah, C. Wang, J. Lu, T. Wu, T. Li, C. Wang, R. Shahbazian-Yassar, L. Hu, *Nat. Nanotechnol.* **2019**, *14*, 851.

[33] A. Angulo, P. van der Linde, H. Gardeniers, M. Modestino, D. F. Rivas, *Joule* **2020**, *4*, 555.

[34] X. Zhao, H. Ren, L. Luo, *Langmuir* **2019**, *35*, 5392.

[35] V. Raghavan, *J. Phase Equilib.* **1994**, *15*, 428.

[36] J. J. Lander, H. E. Kern, A. L. Beach, *J. Appl. Phys.* **1952**, *23*, 1305.

[37] B. Deng, Z. Wang, W. Chen, J. Tianci Li, D. Xuan Luong, R. A. Carter, G. Gao, B. I. Yakobson, Y. Zhao, J. M. Tour, *Nat. Commun.* **2022**, *13*, 262.

[38] P. H. Lu, D. G. Xie, B. Y. Liu, F. Ai, Z. R. Zhang, M. S. Jin, X. F. Zhang, E. Ma, J. Li, Z. W. Shan, *Extreme Mech. Lett.* **2021**, *49*, 101463.

[39] S. T. Hunt, M. Milina, A. C. Alba-Rubio, C. H. Hendon, J. A. Dumesic, Y. Román-Leshkov, *Science* **2016**, *352*, 974.

[40] B. Han, K. A. Stoerzinger, V. Tileli, A. D. Gamalski, E. A. Stach, Y. Shao-Horn, *Nature Mater.* **2017**, *16*, 121.

[41] T.-H. Shen, L. Spillane, J. Vavra, T. Ha, M. Pham, J. Peng, Y. Shao-Horn, V. Tileli, *J. Am. Chem. Soc.* **2020**, *142*, 15876.

[42] J. Jiang, F. Sun, S. Zhou, W. Hu, H. Zhang, J. Dong, Z. Jiang, J. Zhao, J. Li, W. Yan, M. Wang, *Nat. Commun.* **2018**, *9*, 2885.

[43] M. B. Stevens, L. J. Enman, E. H. Korkus, J. Zaffran, C. D. M. Trang, J. Asbury, M. G. Kast, M. Caspary Toroker, S. W. Boettcher, *Nano Res.* **2019**, *12*, 2288.

[44] M. S. Burke, M. G. Kast, L. Trotochaud, A. M. Smith, S. W. Boettcher, *J. Am. Chem. Soc.* **2015**, *137*, 3638.

[45] N. B. Velhal, N. D. Patil, A. R. Shelke, N. G. Deshpande, V. R. Puri, *J. Appl. Phys.* **2015**, *5*, 97166.

[46] S. Singhal, S. Bhukal, J. Singh, K. Chandra, S. Bansal, *J. Nanotechnol.* **2011**, *2011*, 930243.

[47] T.-H. Shen, L. Spillane, J. Peng, Y. Shao-Horn, V. Tileli, *Nat. Catal.* **2022**, *5*, 30.

[48] J. G. Speight, *Environmental Inorganic Chemistry for Engineers*, Butterworth-Heinemann, Oxford **2017**.

[49] Y. Zhu, L. Zhang, B. Zhao, H. Chen, X. Liu, R. Zhao, X. Wang, J. Liu, Y. Chen, M. Liu, Y. M. Zhu, H. J. Chen, X. Liu, J. Liu, Y. Chen, L. Zhang, B. T. Zhao, M. L. Liu, R. Zhao, X. W. Wang, *Adv. Funct. Mater.* **2019**, *29*, 1901783.

[50] D. Zhen, B. Zhao, H.-C. Shin, Y. Bu, Y. Ding, G. He, M. Liu, D. X. Zhen, B. T. Zhao, Y. F. Bu, Y. Ding, M. L. Liu, G. He, H. Shin, *Adv. Mater. Interfaces* **2017**, *4*, 1700146.

[51] N. Li, R. G. Hadt, D. Hayes, L. X. Chen, D. G. Nocera, *Nat. Commun.* **2021**, *12*, 4218.

[52] Z. Chen, J. Wang, D. Chao, T. Baikie, L. Bai, S. Chen, Y. Zhao, T. Chien Sum, J. Lin, Z. Shen, *Sci. Rep.* **2016**, *6*, 25771.

[53] Z. Xiao, H. Wu, H. Zhong, A. Abdelhafiz, J. Zeng, *Nanoscale* **2021**, *13*, 13896.

[54] Z. Xiao, Y. Jiang, H. Wu, H. Zhong, H. Song, A. Abdelhafiz, J. Zeng, *J. Alloys Compd.* **2021**, *877*, 160221.

[55] B. Zhao, L. Zhang, Q. Zhang, D. Chen, Y. Cheng, X. Deng, Y. Chen, R. Murphy, X. Xiong, B. Song, C. P. Wong, M. S. Wang, M. Liu, *Adv. Energy Mater.* **2018**, *8*, 1702247.

[56] J. il Choi, A. Abdelhafiz, P. Buntin, A. Vitale, A. W. Robertson, J. Warner, S. S. Jang, F. M. Alamgir, *Adv. Funct. Mater.* **2019**, *29*, 1902274.

[57] X. Zhong, an. Zhu, W. Dai, J. Yu, T. Lu, Y. Pan, *New J. Chem.* **2022**, *46*, 8398.

[58] L. Sharma, N. Kumar Katiyar, A. Parui, R. Das, R. Kumar, C. Sekhar Tiwary, A. K. Singh, A. Halder, K. Biswas, *Nano Res.* **2022**, *15*, 4799.

[59] L. Sharma, N. Kumar Katiyar, A. Parui, R. Das, R. Kumar, C. S. Tiwary, A. K. Singh, A. Halder, K. Biswas, *Nano Res.* **2022**, *15*, 4799.

[60] J. Abed, S. Ahmadi, L. Laverdure, A. Abdellah, C. P. O'Brien, K. Cole, P. Sobrinho, D. Sinton, D. Higgins, N. J. Mosey, S. J. Thorpe, E. H. Sargent, *Adv. Mater.* **2021**, *33*, 2103812.

[61] M. Bernt, A. Hartig-Weiß, M. Fathi Tovini, H. A. El-Sayed, C. Schramm, J. Schrö Ter, C. Gebauer, H. A. Gasteiger, *Chem. Ing. Tech.* **2020**, *92*, 31.

[62] G. Li, L. Anderson, Y. Chen, M. Pan, P.-Y. A. Chuang, *Sustainable Energy Fuels* **2018**, *2*, 237.

[63] A. Grimaud, O. Diaz-Morales, B. Han, W. T. Hong, Y.-L. Lee, L. Giordano, K. A. Stoerzinger, M. T. M. Koper, Y. Shao-Horn, *Nat. Chem.* **2017**, *9*, 457.

[64] X. Xie, L. Du, L. Yan, S. Park, Y. Qiu, J. Sokolowski, W. Wang, Y. Shao, *Adv. Funct. Mater.* **2022**, *32*, 2110036.

[65] Z. Lu, G. Chen, Y. Li, H. Wang, J. Xie, L. Liao, C. Liu, Y. Liu, T. Wu, Y. Li, A. C. Luntz, M. Bajdich, Y. Cui, *J. Am. Chem. Soc.* **2017**, *139*, 52.

[66] Y. Zhu, W. Zhou, J. Yu, Y. Chen, M. Liu, Z. Shao, *Chem. Mater.* **2016**, *28*, 1691.

[67] K. Cysewska, M. Zając, M. Łapiński, J. Karczewski, M. K. Rybarczyk, B. Kamecki, P. Jasiński, S. Molin, *Energy Technol.* **2021**, *9*, 2100688.

[68] F. Song, M. M. Busch, B. Lassalle-Kaiser, C. S. Hsu, E. Petkucheva, M. Bensimon, H. M. Chen, C. Corminboeuf, X. Hu, *ACS Cent. Sci.* **2019**, *5*, 558.

[69] S. Yeo, A. T. Bell, *J. Am. Chem. Soc.* **2011**, *133*, 5587.

[70] N. H. Chou, P. N. Ross, A. T. Bell, T. D. Tilley, *ChemSusChem* **2011**, *4*, 1566.

[71] Y.-J. Tang, C.-H. Liu, W. Huang, X.-L. Wang, L.-Z. Dong, S.-L. Li, Y.-Q. Lan, *ACS Appl. Mater. Interfaces* **2017**, *9*, 16977.

[72] B. Deng, Z. Wang, W. Chen, J. Tianci Li, D. Xuan Luong, R. A. Carter, G. Gao, B. I. Yakobson, Y. Zhao, J. M. Tour, *Nat. Commun.* **2022**, *13*, 262.

[73] A. A. Abdelhafiz, M. A. Ganzoury, A. W. Amer, A. A. Faiad, A. M. Khalifa, S. Y. Alqaradawi, M. A. El-Sayed, F. M. Alamgir, N. K. Allam, *Phys. Chem. Chem. Phys.* **2018**, 20, 10258.

[74] Z. Jia, T. Yang, L. Sun, Y. Zhao, W. Li, J. Luan, F. Lyu, L.-C. Zhang, J. J. Kruzic, J.-J. Kai, J. C. Huang, J. Lu, C. T. Liu, *Adv. Mater.* **2020**, *32*, 2000385.

[75] Y. Zhu, W. Zhou, J. Sunarso, Y. Zhong, Z. Shao, *Adv. Funct. Mater.* **2016**, *26*, 5862.